



Finite Element Analysis and Electromagnetic Field Optimization of Linear Synchronous Motor in High-Speed Maglev Systems

Maozhenning Yang¹, Yougang Sun^{1,2*}, Junqi Xu², Bing Sun³

¹ Institute of Rail Transit, Tongji University, 201804 Shanghai, China

² Maglev Transportation Engineering R&D Center, Tongji University, 201804 Shanghai, China

³ Department of Mechanical Engineering, University of Victoria, V8P 5C2 Victoria, Canada

* Correspondence: Yougang Sun (1989yoga@tongji.edu.cn)

Received: 07-02-2023

Revised: 07-28-2023

Accepted: 08-08-2023

Citation: M. Z. N. Yang, Y. G. Sun, J. Q. Xu, and B. Sun, "Finite element analysis and electromagnetic field optimization of linear synchronous motor in high-speed maglev systems," *Mechatron. Intell Transp. Syst.*, vol. 2, no. 3, pp. 117–130, 2023. <https://doi.org/10.56578/mits020301>.



© 2023 by the author(s). Published by Acadlore Publishing Services Limited, Hong Kong. This article is available for free download and can be reused and cited, provided that the original published version is credited, under the CC BY 4.0 license.

Abstract: Amidst the evolving dynamics of modern economic life, there emerges an escalating demand for faster modes of travel. In response, advancements in the realm of high-speed maglev train technology, targeting speeds of up to 600 km/h, are being persistently pursued in China. Central to ensuring the stable operation of these high-speed trains is a thorough understanding of the inherent magnetic fields and their electromagnetic interactions during high-speed transits. In this context, the Long Stator Linear Synchronous Motor (LSM) of Tongji University's maglev prototype is investigated. Through an analytical lens, a simplified model of LSM was dissected using the energy method. The distribution patterns of air gap magnetic flux were then ascertained through Fourier transformation coupled with the equivalent current layer, culminating in the derivation of a theoretical equation for electromagnetic forces. A two-dimensional finite element model subsequently shed light on the magnetic induction intensity distribution intricacies inherent to the long stator linear motor. Concurrently, potential end effects impinging on the motor's performance were explored. This comprehensive analysis further revealed the interplay between electromagnetic force, excitation current, and armature current. The observations encapsulated distinct magnetic field distribution patterns, nonlinear interdependencies between current and magnetic force, and pronounced saturation characteristics. Collectively, these findings furnish a robust theoretical scaffold for the simplification and optimization of electromagnetic forces in high-speed maglev systems.

Keywords: High-speed maglev systems; LSM; Finite element analysis (FEA); Electromagnetic field optimization

1 Introduction

Amid the evolving economic landscape, a heightened demand for rapid transportation modes has arisen. China's research endeavors into high-speed magnetic levitation (maglev) trains have seen substantial progress. Notably, in May 2019, CRRC Sifang unveiled its groundbreaking 600 km/h high-speed maglev train. By 2020, successful trials of a 600 km/h high-speed maglev test vehicle were conducted on the Tongji University maglev test line in Shanghai, and by July 2021, a domestically developed 600 km/h high-speed maglev train was launched in Qingdao [1–4]. Ensuring the stability of such rapid maglev systems necessitates a thorough exploration into the magnetic fields and electromagnetic interplays during high-velocity operations [5].

Studies on the EMS-type LSM have been conducted by numerous scholars both domestically and abroad. Due to the open slots on the surface of the long stator that hold single-turn three-phase windings, the resultant cogging effect is considered the main cause of fluctuations in traction and levitation forces [6, 7]. Analysis of the vertical force variation under the cogging effect in permanent magnet linear motors was conducted by Xia et al. [8], who used the Maxwell tensor method and finite element analysis to study the effect of pole-arc coefficient and tooth tip width. Wang et al. [9] provided a relatively accurate derivation of the relative magnetic permeability function in the air gap, considering the Dirichlet law and winding characteristics. Liu et al. [10] examined the influence of stator segmentation patterns on the air gap magnetic permeability function, while Zhang and Lu [11] designed a skewed tooth scheme to reduce thrust fluctuation caused by stator cogging effects, optimizing parameters through simulation.

However, most LSM cogging effect studies have concentrated on the analysis of stator cogging effects, with less attention paid to the impact generated by the vehicle's magnetic poles. The characteristics of motor traction and levitation forces are also key performance indicators. The majority of these studies have predominantly utilized finite element analysis in combination with theoretical results from simplified models for comparison [12–19]. This approach enables the exploration of a variety of factors influencing LSM performance. Three-dimensional motor model simulation methods were employed by other researchers, providing a more nuanced view of LSM behaviors [20]. In a notable first, Maxwell finite element simulation software was used to analyze long stator winding fault conditions [21], contributing a new perspective to the field.

Cao et al. [22] not only analyzed the coupled characteristics of traction and levitation forces under different armature currents and power angles but also examined the effect of aerodynamic lift on these characteristics. It concluded that, under current aerodynamic characteristics, there is a maximum speed for constant-guidance maglev trains. Despite these advancements, there is a noticeable lack of research on the magnetic field and electromagnetic relationships of high-speed maglev trains.

The magnetic field, pivotal for maglev train suspension, plays an indispensable role in assuring the safe and consistent control of high-speed maglev trains. As the crux of the maglev train suspension mechanism, the magnetic field guarantees stable suspension, orchestrates train alignment, dampens external perturbations, and directly influences the system's stability, agility, and safety. In the present study, an analytical magnetic field model of the motor was formulated. Key parameters such as the effective air gap, armature variables, levitation force, and traction force were meticulously computed. With the assistance of ANSYS Electronic Desktop electromagnetic field FEA software, a two-dimensional motor model was employed to discern thrust and levitation dynamics under variant stator currents and disparate linear generator loads. This investigation unveiled salient features encompassing magnetic field distribution, intricate nonlinear associations between current and magnetic force, and saturation characteristics. This exploration furnishes foundational theoretical insights for refining the electromagnetic force in 600 km/h high-speed maglev trains.

2 Fourier Analysis of LSM's Equivalent Current Layer

2.1 Equivalent Current Layer

To model the magnetic field, an energy-based approach has been utilized wherein the magnetic field is stratified. Within this stratification, an infinitesimally thin layer representing the stator and excitation current, termed the "equivalent current layer," has been introduced. By leveraging the Laplace equation for a curl-free field, the distribution of the magnetic field across each stratified region can be discerned. For the sake of streamlining the analytical process, the following assumptions were incorporated:

- Analysis of the magnetic field and force was confined to a two-dimensional plane.
- Both the stator and rotor were assumed to possess magnetic materials of identical, infinite magnetic permeability.
- Only the fundamental magnetic field for both armature and poles was considered in the analysis.
- The potential effects of magnetic saturation and eddy currents were overlooked during the computation phase.

Given a three-phase winding with N turns per phase, a phase difference of 120° between each successive phase, and a designated current density J_x (with x adopting values of a, b, c), alongside parameters like stator slot width b_s , slot pitch a_s , and pole pitch τ_s , the Fourier expansion of the current density can be articulated as:

$$J_X(x) = \begin{cases} -\sum_{n=1}^{\infty} \frac{4J_a}{n\pi} \sin \frac{n\pi}{2} \sin \frac{n\pi b_s}{2\tau_s} \sin \frac{n\pi}{\tau_s} x \\ -\sum_{n=1}^{\infty} \frac{4J_b}{n\pi} \sin \frac{n\pi}{2} \sin \frac{n\pi b_s}{2\tau_s} \sin \frac{n\pi}{\tau_s} \left(x - \frac{2}{3}\tau_s\right) \\ -\sum_{n=1}^{\infty} \frac{4J_c}{n\pi} \sin \frac{n\pi}{2} \sin \frac{n\pi b_s}{2\tau_s} \sin \frac{n\pi}{\tau_s} \left(x + \frac{2}{3}\tau_s\right) \end{cases} \quad (1)$$

Subsequently, the cumulative three-phase currents were computed, and the fundamental wave was isolated, resulting in:

$$J_s(x) = J_a(x) + J_b(x) + J_c(x) = \frac{6NI \sin \frac{\pi b_s}{2\tau_s}}{\pi b_s} \sin(\omega t - \pi x/\tau_s) \quad (2)$$

Building on the premise wherein the stator pole pitch mirrors the vehicle excitation pole pitch, the Fourier expansion of the excitation current density is described as:

$$J_p(x) = -\frac{8N_p I_P \sin \frac{\pi \tau_p}{2\tau_s}}{\pi \tau_p} \sin(\pi x/\tau_s) \quad (3)$$

It's noteworthy to highlight that while varying stator and rotor pole pitches might be harnessed in real-world LSM applications with the objective of minimizing electromagnetic force oscillations, the theoretical computations stemming from equal and unequal pole pitches demonstrate negligible divergence, particularly in the fundamental wave outcome of the Fourier transformation. As such, in this discourse, attention is solely dedicated to the calculations associated with equal pole pitch.

2.2 Modeling of Tooth-Slot Permeability

To model the tooth-slot structure, which comprises both the air gap and iron core mediums, media with differing magnetic permeabilities in the x and y directions were employed. Herein, magnetic permeabilities in the x and y directions are represented as μ_x and μ_y , respectively. The magnetic permeability of air is denoted as μ_0 , while that of the stator iron core is expressed as μ_{Fe} . Drawing upon magnetic circuit principles, the following relationships were derived:

$$\begin{cases} \mu_x = \frac{\mu_0 \mu_{Fe} (b_s + a_s)}{b_s \mu_{Fe} + a_s \mu_0} \\ \mu_y = \frac{b_s \mu_{Fe} + a_s \mu_0}{b_s + a_s} \end{cases} \quad (4)$$

2.3 Analysis of Electromagnetic Fields

As shown in Figure 1, the layered magnetic field model of LSM is presented.

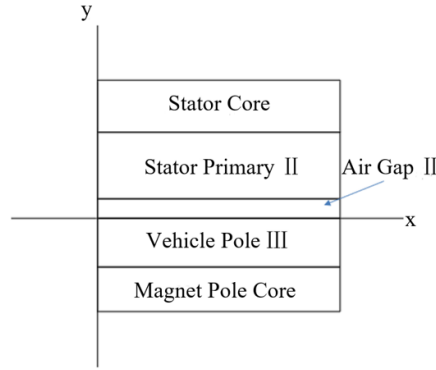


Figure 1. LSM Layered magnetic field representation

In this model, a layered calculation method was applied. The magnetic fields generated exclusively by the stator current layer in regions I and III were determined, and the magnetic fields attributed to the vehicle excitation current layer were subsequently superimposed. This approach enabled the quantification of magnetic fields in each region, facilitating the computation of the electromagnetic forces therein.

For instance, when focusing on the excitation current layer, the Laplace equation in air-gap region I, influenced only by the vehicle's magnetic pole, is represented as:

$$\begin{aligned} \frac{\partial^2 \Phi_1}{\partial x^2} + \frac{\partial^2 \Phi_1}{\partial y^2} &= 0 \\ \frac{\partial \Phi_1}{\partial x} \Big|_{(y=0)} &= J_2 \end{aligned} \quad (5)$$

Taking into account solely the fundamental wave, solutions were derived from the established boundary conditions. The results are:

$$\begin{cases} B_{1x} = \mu_0 C \sin Cx \left(A \operatorname{sh} Cy + C \frac{8N_p I_R}{\pi \tau_m} \sin \frac{C\tau_m}{2} \operatorname{ch} Cy \right) \\ B_{1y} = -\mu_0 C \cos Cx \left(A \operatorname{ch} Cy + C \frac{8N_p I_R}{\pi \tau_m} \sin \frac{C\tau_m}{2} \operatorname{sh} Cy \right) \\ C = \frac{\pi}{\tau_s} \end{cases} \quad (6)$$

The procedures for calculating the composite magnetic field in other regions were not elaborated further within this section. The formula derived for electromagnetic force computation via the magnetic field energy method is:

$$F = J * B - 0.5H^2 gradu \quad (7)$$

Upon evaluation, when the power angle is set at 90° , the expressions for the traction and levitation forces of the linear motor were identified as [23, 24]:

$$\begin{cases} F_x = \frac{pL_1\mu_0J_EJ_p\tau^2}{\pi h_s} \frac{shCh_s}{shh_s(h_s+g_0)} \\ F_y = \frac{b_zp\mu_0\tau^3L^2J_p^2}{2t_zg_0^2\pi^2} \left(\frac{shCh_s}{shh_s(h_s+g_0)} - 1 \right)^2 \end{cases} \quad (8)$$

These equations highlight that the traction force is directly influenced by the product of the stator and excitation currents, while the levitation force is dependent on the square of the excitation current. Both forces were observed to amplify as the air gap, represented as g_0 , diminishes.

3 Two-Dimensional FEA of LSM Motor Using ANSYS

The electromagnetic tool, ANSYS Electronics Desktop – the latest rendition of ANSYS Maxwell – was selected for its proven efficacy in low-frequency phenomena and device analyses. Notably, its compatibility with other ANSYS electromagnetic tools facilitates seamless integration within a multi-physics analytical platform. For the context of this research, the structural design of the high-speed maglev train linear synchronous motor (LSM) from Tongji University's Maglev Center was employed, drawing inspiration from the German TR08 maglev train and incorporating several structural optimizations. A visual representation of this model is provided in Figure 2.

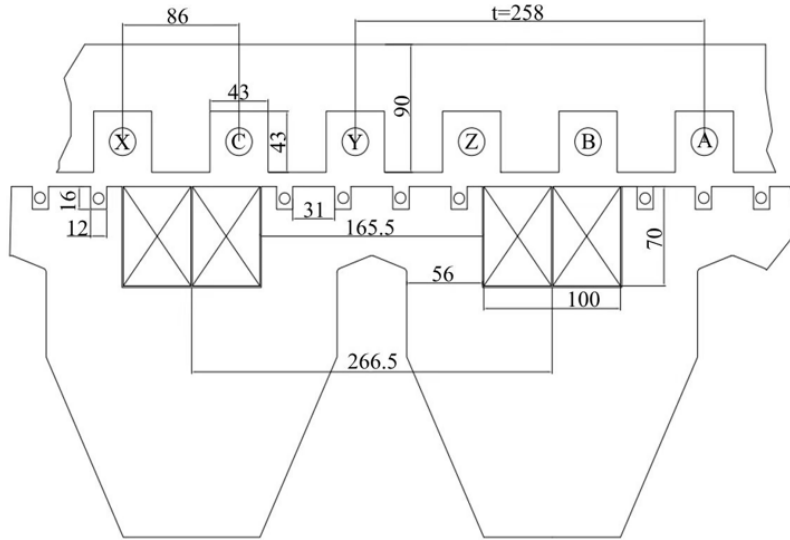


Figure 2. Structural parameters of the LSM's two-dimensional model

To ensure a consistent terminological framework throughout this study, the following definitions were adopted:

- The X-axis is identified with the direction of the train's motion, with motor parameters along this axis being classified as 'length'.

- The Y-axis corresponds to the train's levitation direction, with parameters in this direction designated as 'height'.

- Lastly, the Z-axis signifies the train's guidance direction, with the motor's size in this axis termed as 'width'.

A summary of the primary parameters is tabulated in Table 1, Table 2 and Table 3.

A two-dimensional transient field simulation method was adopted for all models. In order to examine the traction magnetic field's impact on electromagnetic force under decoupling conditions, a power angle of 90° had to be maintained in the model. This condition was met by modulating the initial phase angle of alternating current to ensure the direct-axis current (id) of the stator was zero. As such, the magnetic pole axis at the initial transient simulation position was aligned with the stator's magnetic pole axis. Parameterized simulations were subsequently conducted, with the A-phase alternating current initial phase being the primary variable. The phase angle maximizing the traction force was identified and used as the initial phase angle. The desired power angle of 90° was achieved with an A-phase current phase angle of 210 degrees, B-phase angle of 90 degrees, and a C-phase angle of -30 degrees.

Subsequently, a two-dimensional CAD model, representing these parameters, is showcased in Figure 3.

(1) Finite Element Model Geometry and Material Configurations

Table 1. Main parameters of the stator armature primary

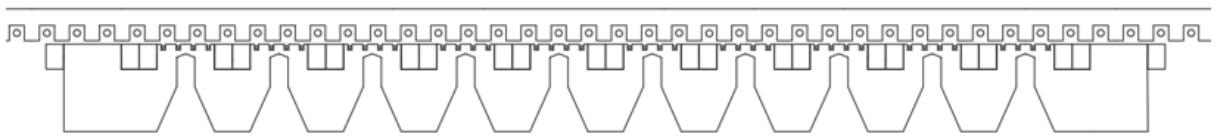
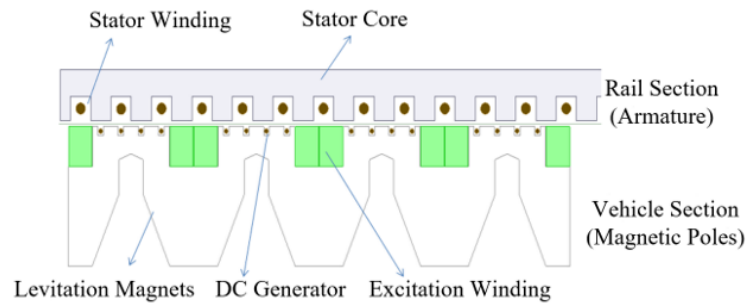
Name	Value	Unit
Armature Length	1200	m
Armature Slot Height	43	mm
Armature Slot Length	43	mm
Armature Core Width	184	mm
Armature Core Height	90	mm
Slot Number per Pole per Phase	1	/
Turns per Slot	1	/
Armature Pole Pitch	258	mm
Stator Current	1200	A
Conductor Area	300	mm ²

Table 2. Main parameters of the vehicle's secondary

Name	Value	Unit
Pole Pitch	266.5	mm
Main Pole Length	170	mm
End Pole Length	85	mm
Secondary Core Width	168	mm
Secondary Height	247	mm
Pole Length	163	mm
Pole Height	70	mm
Magnetic Yoke Length	215	mm
Excitation Coil Length*Height	50*70	mm
Excitation Coil Current	20	A
Excitation Coil Turns	270	/

Table 3. Main parameters of the onboard linear generator

Name	Value	Unit
Generator Slot Length*Height	12*16	mm
Generator Tooth Length	43	mm
Turns per Generator Slot	28	/

**Figure 3.** Comprehensive depiction of the LSM's two-dimensional model**Figure 4.** Two-dimensional finite element simulation model of 4 magnetic poles

A simplified motor, comprising 4 magnetic poles and a 10mm air gap, served as the basis for the finite element

simulation, as depicted in Figure 4. The long stator core and excitation magnetic pole core were recognized as being composed of 0.5 mm/piece silicon steel laminations. Therefore, the nonlinear material silicon steel sheet (DW470-50) was utilized. Building upon the properties of DW465-50 in the ANSYS material library, the lamination type was set as "Lamination," featuring a stacking factor of 0.97 and stacking direction v3, aligning with the z-axis in Cartesian coordinates. This stacking factor represents the ratio between the magnetic conduction length and the total length, considering that silicon steel sheets typically comprise magnetic cold-rolled steel and non-magnetic insulating material. The conductivity of these sheets was determined to be 2000000 S/m, encompassing eddy current losses in the core loss calculation.

(2) Excitation Sources and Parameter Settings for Primary and Secondary Windings

Electricity for the stator three-phase current of the high-speed maglev train's linear motor was derived from terrestrial power stations, with the effective current fluctuating based on the train's speed. Current frequency was derived from the equation $f = v/2\tau_r$. For a transient field simulation at 100m/s, the default effective current value was set at 1200A, with a frequency of 100/0.516Hz. The winding sorting method was assigned as A-Z-B-X-C-Y, and the current type was defined as "Stranded". The alternating currents loaded onto the three-phase winding were specified as follows:

$$\begin{aligned} i_A &= 1200 * \text{sqrt}(2) * \sin(2 * \pi * (100/0.516) * \text{time} + \pi * 7/6) \\ i_B &= 1200 * \text{sqrt}(2) * \sin(2 * \pi * (100/0.516) * \text{time} + \pi * 1/2) \\ i_C &= 1200 * \text{sqrt}(2) * \sin(2 * \pi * (100/0.516) * \text{time} - \pi * 1/6) \end{aligned} \quad (9)$$

(3) Secondary Movement Parameters, Motion Boundaries, and Solution Configurations

A rectangular region, termed Region A, was initially employed to encase the secondary moving magnetic pole, permitting Region A to execute unified motion within the stipulated motion range during transient calculations. The boundary of Region A was marginally extended, slightly exceeding 2 mm past the secondary winding boundary. Subsequently, a secondary motion area (Region B), spanning 1500 mm, was introduced, with its movement aligned with the positive X-direction of the Cartesian coordinate system. Parameters, such as the solution's initial position and maximum position, were configured as mentioned. The "Region" boundary condition was defined as "Vector-Potential". Transient analyses factored in a maglev train speed of 360 km/h, with designated time intervals. The origin of the Cartesian coordinate system for the motor model was aligned with the stator's far-left position, with transient simulations commencing from this origin. A total of 61 transient analysis points were plotted, enveloping a cumulative distance equivalent to two stator pole pitches in 5.16 ms. The model depth was fixed at 180mm, corresponding to the core's width, and mesh refinement was conducted, as illustrated in the finite element model grid division (Figure 5) for the two-dimensional linear motor.

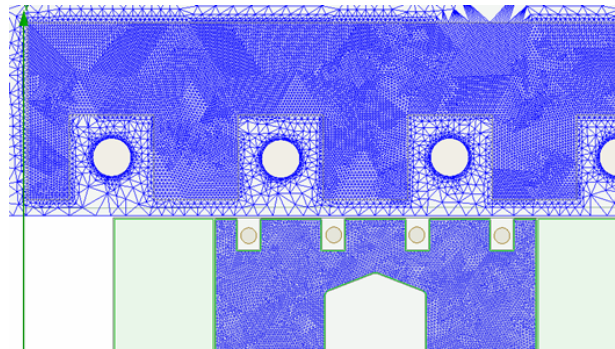


Figure 5. Mesh division of the two-dimensional linear motor's finite element model

4 Simulation Analysis of Electromagnetic Fields in LSM Motors

4.1 Examination of Magnetic Induction Intensity Distribution

In a departure from traditional wheel-track transportation systems, magnetic levitation trains harness electromagnetic forces for vehicle levitation and propulsion. Specifically, in Electromagnetic Suspension (EMS) systems, the levitation of the vehicle is achieved through the excitation of electromagnets positioned beneath the tracks equipped with a three-phase armature stator. The interaction between this stator core and the vehicular levitation electromagnets yields attractive forces that keep the vehicle elevated.

Within the electromagnetic stator, the three-phase current produces a moving magnetic field. This field engages in an interactive dance with the vehicle's magnetic poles, creating forward momentum. Post-processing procedures

on the finite element model yielded visual interpretations in the form of magnetic induction intensity cloud diagrams and magnetic force line distribution cloud diagrams, which are illustrated in Figure 6 and Figure 7. These diagrams effectively capture spatial variations and intensity gradients of the magnetic field. Such a design is intuitive: regions of high intensity are typically rendered in warmer hues such as red, whereas lower intensities might be depicted in cooler shades like blue.

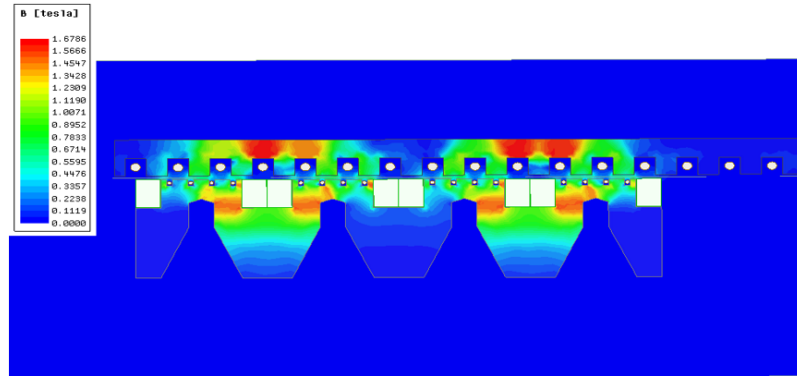


Figure 6. Visualization of magnetic induction intensity in a two-dimensional long-stator linear motor

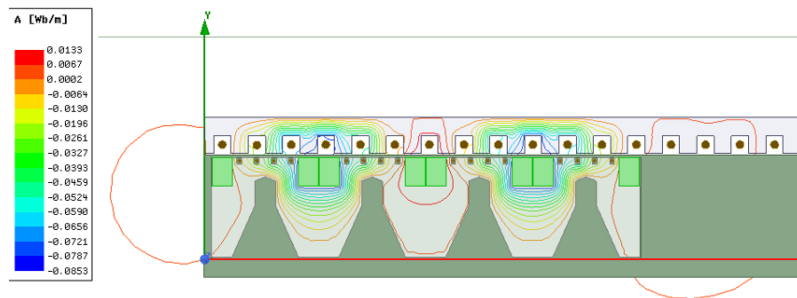


Figure 7. Magnetic force line distribution in a two-dimensional long-stator linear motor

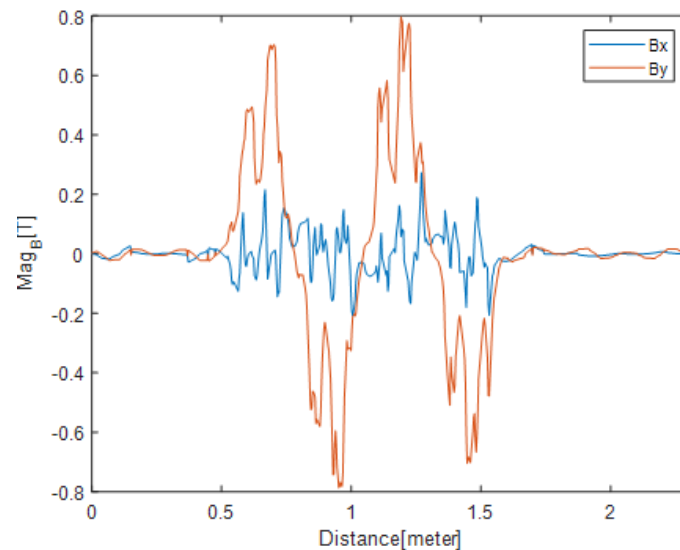


Figure 8. Cross-sectional distribution of magnetic induction intensities b_x and b_y at a 5.16 ms position along motor's length

An examination of Figure 7 reveals that magnetic force lines follow a looped trajectory. Beginning their journey in the stator, they traverse the air gap to eventually connect with the secondary excitation magnetic poles, with minor leakages noted within this gap. A distinct red zone in the stator is discernible, indicating the three-phase winding's

magnetic pole distribution. It is notable that during transit, a consistent misalignment exists between these and the excitation magnetic poles. This misalignment is crucial, playing a pivotal role in generating forward traction. Concurrently, the highest magnetic induction intensity observed within the motor was approximately 1.8T, indicating a persistent unsaturated operational state.

In a granular observation at a specific temporal juncture, magnetic induction intensities B_x and B_y at the air gap's epicenter along the motor's longitudinal axis are elucidated in Figure 8 and Figure 9. The magnetic induction intensity predominantly gravitated in the Y direction (corresponding to levitation force), peaking at around 0.79T. A fluctuating, yet comparably diminutive, magnetic induction component was also identified in the X direction (pertaining to the traction force). A series of discernible troughs in the magnetic induction intensity distribution at regions corresponding to the stator tooth slots suggests an increase in magnetic reluctance at these sites. This, in turn, attenuates the levitation force.

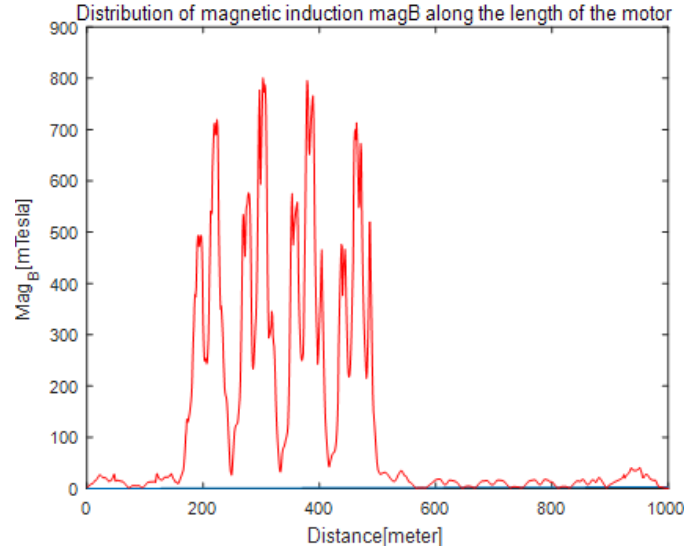


Figure 9. Total magnetic induction intensity distribution in the air gap at a 5.16 ms position along motor's length

4.2 Long-Stator Effects in LSM Motors: An Examination

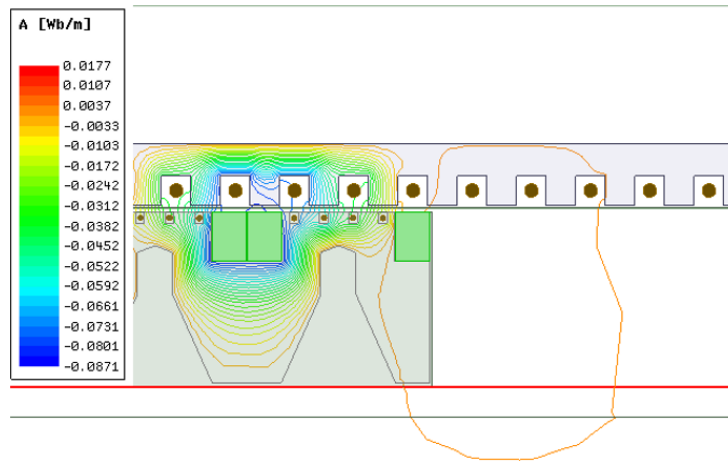


Figure 10. Visualization of minor magnetic leakage at the terminal of the motor

Within long-stator linear synchronous motors, a distinction is observed wherein the length of the secondary or the vehicle's magnetic poles remains finite. Conversely, the primary length, represented by the three-phase stator windings serving as the track, significantly surpasses that of the secondary. As a result, distinct terminations – a beginning and an end – are inherent to each full vehicle magnetic pole. Such demarcations culminate in a distinctive longitudinal end effect, emblematic of long-stator linear motors.

Of note, both the vehicle's magnetic poles and the stator have been constructed using 0.5mm silicon steel laminations. It is suggested that due to this composition, eddy currents birthed by the end effect are essentially

negligible. Furthermore, the impact exerted by these eddy currents on the air gap magnetic field appears to be inconsequential. As elucidated in Figure 10, magnetic leakage at the terminal of the motor is relatively minimal.

To fully comprehend the implications of the longitudinal end effect, it is crucial to delve deeper into its genesis. The structural difference in length between the primary and secondary components plays a pivotal role. Yet, the negligible effect of eddy currents, despite the pronounced difference in lengths, speaks volumes about the efficacy of the materials employed. Further investigations could potentially illuminate strategies to further minimize even this minor magnetic leakage, optimizing LSM motor performance.

4.3 Electromagnetic Force Dependency on Excitation and Armature Currents

The relationship between the electromagnetic forces and the excitation and armature currents remains a pivotal area of investigation in linear motor applications. For this discourse, a detailed examination of the traction force and levitation force over time, with set parameters of excitation current at 20A and armature current at 1200A, has been undertaken.

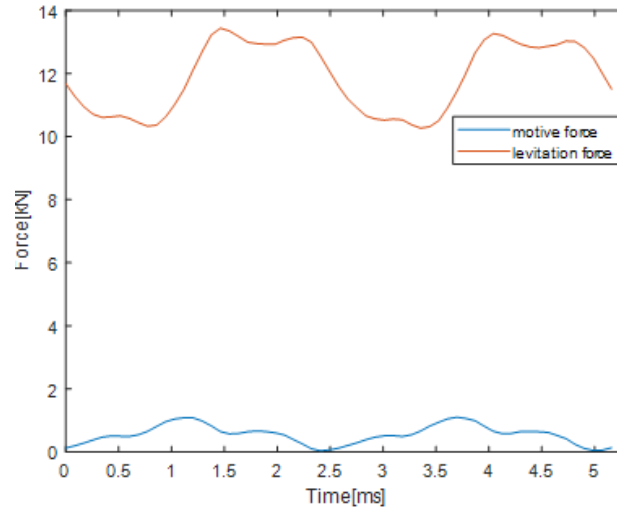


Figure 11. Waveform of traction force and levitation force over time

Figure 11 depicts the time-based waveform alterations of both forces. A variance in the traction force, for the 4-pole linear motor, is identified to oscillate between 0.035 and 1.1009 kN. In contrast, the levitation force exhibits fluctuations between 10.26 and 13.43 kN, thus demonstrating a magnitude approximately ten times that of the traction force. It was discerned that the air gap magnetic field is dominated by the 5th and 7th harmonic components. Interactions between these harmonics and the three-phase armature current induce traction force fluctuations, occurring at a frequency six times the fundamental. A formula detailing the computation of traction force fluctuations due to slotting effects, as delineated in reference [24], is:

$$N_{\tau} = \frac{LCM(2pN_s)}{p} \quad (10)$$

where, p symbolizes the number of pole pairs, with N_s representing the stator slots. With an established model where $p = 1$ and $N_s = 6$, the harmonic components of traction force are computed to be six times the foundational frequency. Validation of this was found in Figure 11, showcasing traction force harmonic values of 6, 12, and 18—consistent with prior theoretical analyses.

In practical applications, such as maglev trains, symmetrically positioned excitation poles are found on either side. A 180° phase difference in the traction forces on both ends, if achieved by controlled armature current phase, might attenuate the slotting effect, subsequently minimizing traction force deviations.

(a) Influence of Excitation Current

With a regulated motor power angle at 90° and a consistent armature current of 1200A, variances in the excitation current were documented between 15A and 30A. Figure 12 and Figure 13 exhibit these traction and levitation force fluctuation curves. Numerical disparities in both forces, subject to excitation current alterations, are tabulated in Table 4. An enhancement in traction and levitation forces was observed with increasing excitation current. No evidence of negative curvatures in the plots was identified, suggesting the absence of core saturation near 30A excitation current. From Maxwell's stress tensor derivations, levitation force calculations, contingent on the magnetic field, are given as:

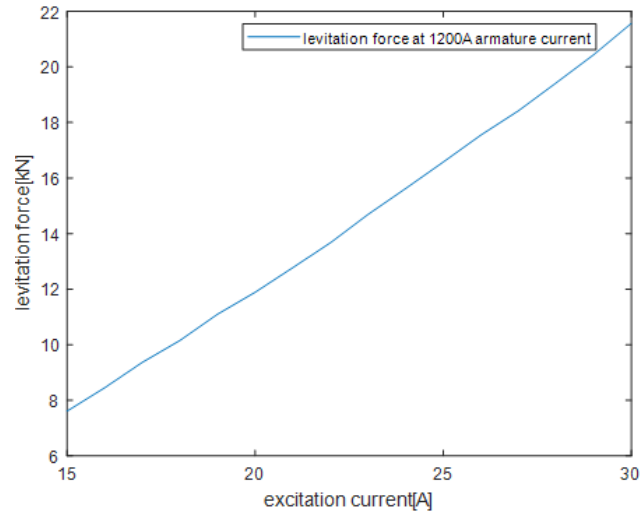


Figure 12. Levitation force waveform from 15A to 30A excitation current

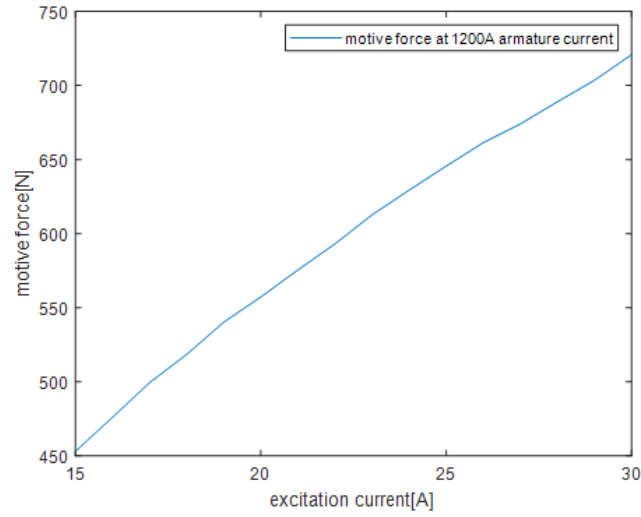


Figure 13. Traction force waveform from 15A to 30A excitation current

Table 4. Key parameters of our model

Excitation Current (A)	Levitation Force (kN)	Motive Force
15	7.60	447.33
16	8.44	470.10
17	9.36	493.15
18	10.15	511.99
19	11.10	533.41
20	11.88	550.21
21	12.77	568.22
22	13.67	585.58
23	14.69	604.87
24	15.62	621.31
25	16.57	637.32
26	17.54	652.92
27	18.42	665.35
28	19.42	680.05
29	20.44	694.29
30	21.57	711.16

$$F_y \approx \frac{p\tau b_e * B_y^2}{4\mu_0} \quad (11)$$

Comparative analyses between theoretical predictions and simulated outcomes revealed significant coherence.

(b) Implications of Armature Current

Maintaining a motor power angle of 90° , an excitation current of 20A, and varying only the armature current in the range of 600A to 1800A, resultant changes were documented in Figure 14 and Figure 15. Here, it was observed that while traction thrust proportionately augmented with increments in three-phase winding current, levitation force increments remained more subdued. The numerical contrasts between levitation and traction forces, influenced by armature current, are presented in Table 5. The disparity in the influence of the levitation force between excitation and armature currents exceeded a tenfold magnitude. These observations imply that, by ensuring a 90° power angle and an invariant air gap magnetic field, modulation of the armature current could effectively decouple and control traction force without significant levitation force perturbation.

Conclusively, the modulation of excitation and armature currents, and their implications on traction and levitation forces, offer invaluable insights into optimization strategies for linear motor applications. The findings pave the way for further in-depth research into decoupling strategies for force control.

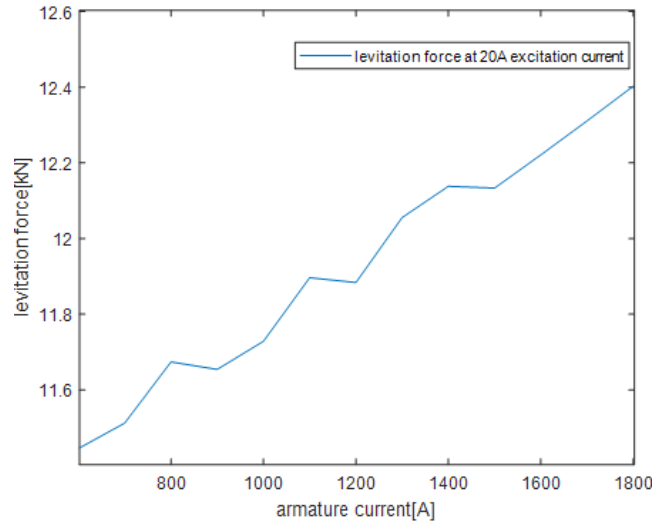


Figure 14. Levitation force waveform from 600A to 1800A armature current

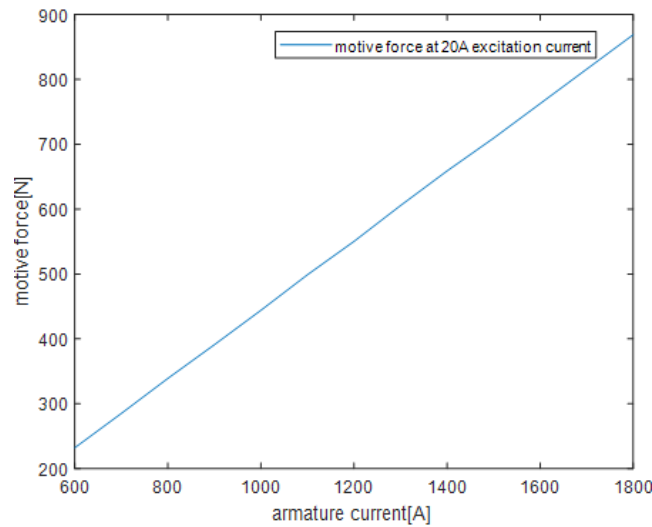


Figure 15. Traction force waveform from 600A to 1800A armature current

Table 5. Numerical variation of levitation and traction forces with armature current

Armature Current (A)	Levitation Force (kN)	Motive Force (N)
600	11.45	232.03
700	11.51	284.99
800	11.67	339.04
900	11.65	391.02
1000	11.73	444.05
1100	11.90	498.90
1200	11.88	550.21
1300	12.06	605.59
1400	12.14	658.97
1500	12.13	709.58
1600	12.22	762.70
1700	12.31	815.83
1800	12.40	868.95

5 Conclusion

In the pursuit of understanding the electromagnetic field dynamics in LSM for the efficient operation of maglev trains, particularly those aiming for 600 km/h speeds, extensive numerical simulations were conducted. Employing both analytical methods and the finite element method to scrutinize the electromagnetic forces, salient insights were derived:

(1) Given an unaltered motor's air-gap magnetic field and a power angle maintained at 90° , the levitation force was discerned to be directly contingent on the excitation current. In parallel, the traction force was ascertained to be linked with the magnitude of the three-phase current.

(2) Examination of the magnetic field lines at the motor's terminus revealed no significant anomalies in distribution patterns. Consequently, for LSMs fabricated using silicon steel sheets as their iron core, both the end effect and the consequent eddy currents were deemed inconsequential.

(3) A consistent trend was observed wherein both the traction and levitation forces augmented progressively with rising excitation currents. Absence of any downward inflection in the waveform curve suggests that core saturation remains elusive at an excitation current proximate to 30A.

(4) An incremental pattern was discerned in the traction thrust, aligning with the surge in the three-phase winding current. Nonetheless, the influence of this current on the levitation force remained subdued. To illustrate, when juxtaposed against the amplified levitation force resultant from augmented excitation current, the influence factor disparity exceeded a magnitude of tenfold. Such findings subtly infer the potential to regulate traction force—by modulating the armature current, while simultaneously preserving the levitation force—as long as the power angle persists at 90° .

It is worth noting that the simulations undertaken in this inquiry exclusively incorporated electromagnetic field considerations, thereby excluding multi-physics field simulation analyses. In real-world scenarios, an elevation in train velocity would invariably culminate in amplified aerodynamic lift. A hypothetical threshold velocity could be envisioned where this aerodynamic lift equates to the gravitational pull on the train. To hone the precision of magnetic field analyses, it is imperative that aerodynamic loads are incorporated into the model, necessitating comprehensive multi-physics field coupling simulation analyses within tools such as ANSYS. This avenue is highlighted as pivotal for forthcoming research endeavors.

Data Availability

The data used to support the findings of this study are available from the corresponding author upon request.

Conflict of Interest

The authors declare that they have no conflicts of interest.

References

- [1] Z. Deng, Z. Liu, H. Li, and W. Zhang, "Development status and prospect of maglev train," *J. Southwest Jiaotong Univ.*, vol. 57, no. 3, pp. 455–474, 2022. <https://doi.org/10.3969/j.issn.0258-2724.20220001>
- [2] F. Li, Y. Sun, J. Xu, Z. He, and G. Lin, "Control methods for levitation system of ems-type maglev vehicles: An overview," *Energies*, vol. 16, no. 7, p. 2995, 2023. <https://doi.org/10.3390/en16072995>

- [3] Y. Sun, Z. He, J. Xu, S. Wenjian, and G. Lin, "Dynamic analysis and vibration control for a maglev vehicle-guideway coupling system with experimental verification," *Mech. Syst. Signal Process.*, vol. 188, p. 109954, 2023. <https://doi.org/10.1016/j.ymssp.2022.109954>
- [4] N. Prasad, S. Jain, and S. Gupta, "Electrical components of maglev systems: Emerging trends," *Urban Rail Transit*, vol. 5, pp. 67–79, 2019. <https://doi.org/10.1007/s40864-019-0104-1>
- [5] Y. Sun, D. Gao, Z. He, and H. Qiang, "Influence of electromagnet-rail coupling on vertical dynamics of EMS maglev trains," *Mechatron. Intell Transp. Syst.*, vol. 1, no. 1, pp. 2–11, 2022. <https://doi.org/10.56578/mits010102>
- [6] Q. Lu, Y. Shen, and Y. Ye, "Development of permanent magnet linear synchronous motors structure and research," *Proc. CSEE*, vol. 39, no. 9, pp. 2575–2588, 2019.
- [7] H. Wang, J. Li, R. Qu, J. Lai, H. Huang, and H. Liu, "Study on high efficiency permanent magnet linear synchronous motor for maglev," *IEEE Trans. Appl. Supercond.*, vol. 28, no. 3, p. 0601005, 2018. <https://doi.org/10.1109/TASC.2018.2796560>
- [8] J. Xia, S. Li, and B. Pen, "Influences of cogging effects on normal force ripple in permanent magnet linear servo motors," *Proc. CSEE*, vol. 35, no. 11, pp. 2847–2853, 2015.
- [9] G. Wang, W. Wei, and J. Liu, "Calculation of air flux density for tr 08," *Trans. China Electrotech. Soc.*, vol. 21, no. 7, pp. 1–4, 2006.
- [10] F. Liu, L. Shi, and Y. Li, "Thrust force calculation of lsm with asymmetric long stator," *In 2009 International Conference on Electrical Machines and Systems, Tokyo, Japan*, pp. 1–4, 2009. <https://doi.org/10.1109/ICEMS.2009.5382807>
- [11] J. Zhang and Q. Lu, "Magnetic-thermal coupled analysis of eletromagnets for medium-speed maglev train," *In 2019 22nd International Conference on Electrical Machines and Systems (ICEMS), Harbin, China*, pp. 1–5, 2019. <https://doi.org/10.1109/ICEMS.2019.8921696>
- [12] J. M. Jo, J. H. Lee, Y. J. Han, C. Y. Lee, and K. S. Lee, "A position estimator using kalman filter with a data rejection filter for a long-stator linear synchronous motor of maglev," *IEEE Access*, vol. 8, pp. 52 443–52 451, 2020. <https://doi.org/10.1109/ACCESS.2020.2981053>
- [13] J. Kang, S. Mu, and F. Ni, "Improved el model of long stator linear synchronous motor via analytical magnetic coenergy reconstruction method," *IEEE Trans. Magn.*, vol. 56, no. 8, pp. 1–13, 2020. <https://doi.org/10.1109/TMAG.2020.3002964>
- [14] R. Leidhold and P. Mutschler, "Speed sensorless control of a long-stator linear synchronous motor arranged in multiple segments," *IEEE Trans. Ind. Electron.*, vol. 54, no. 6, pp. 3246–3254, 2007. <https://doi.org/10.1109/TIE.2007.905941>
- [15] J. M. Jo, S. Y. Lee, K. Lee, Y. J. Oh, S. Y. Choi, C. Y. Lee, and K. Lee, "A position estimator using kalman filter with a data rejection filter for a long-stator linear synchronous motor of maglev," *IEEE Access*, vol. 8, pp. 52 443–52 451, 2020. <https://doi.org/10.1109/ACCESS.2020.2981053>
- [16] H. Wang, J. Li, R. Qu, J. Lai, H. Huang, and H. Liu, "Thrust force calculation of LSM with asymmetric long stator," *IEEE Trans. Appl. Supercond.*, vol. 28, no. 3, p. 0601005, 2018. <https://doi.org/10.1109/TASC.2018.2796560>
- [17] Y. Sun, H. Qiang, L. Wang, W. Ji, and A. Mardani, "A fuzzy-logic system-based cooperative control for the multi-electromagnets suspension system of maglev trains with experimental verification," *IEEE Trans. Fuzzy Syst.*, 2023. <https://doi.org/10.1109/TFUZZ.2023.3257036>
- [18] Y. Sun, J. Xu, C. Chen, and W. Hu, "Reinforcement learning-based optimal tracking control for levitation system of maglev vehicle with input time delay," *IEEE Trans. Instrum. Meas.*, vol. 71, pp. 1–13, 2022. <https://doi.org/10.1109/TIM.2022.3142059>
- [19] Y. Do Chung, C. Y. Lee, and M. H. Jang, "Electromagnetic analysis for multiple hybrid HTS electromagnets interfaced with LSM propulsion system in EMS maglev model," *2014 IEEE International Conference on Industrial Technology (ICIT), Busan, Korea (South)*, pp. 115–120, 2014. <https://doi.org/10.1109/ICIT.2014.6894923>
- [20] M. Fitouri, Y. Bensalem, and M. N. Abdelkrim, "Comparison between 2d and 3d modeling of permanent magnet synchronous motor using fem simulations," *2020 17th International Multi-Conference on Systems, Signals & Devices (SSD), Monastir, Tunisia*, pp. 681–685, 2020. <https://doi.org/10.1109/SSD49366.2020.9364256>
- [21] A. Usman and B. S. Rajpurohit, "Comprehensive analysis of demagnetization faults in BLDC motors using novel hybrid electrical equivalent circuit and numerical based approach," *IEEE Access*, vol. 7, pp. 147 542–147 552, 2019. <https://doi.org/10.1109/ACCESS.2019.2946694>
- [22] X. Cao, Q. Ge, J. Zhu, L. Zhao, and D. Zeng, "Periodic traction force fluctuations suppression strategy of maglev train based on flux linkage observation and harmonic current injection," *IEEE Trans. Transp. Electrification*, vol. 9, no. 2, pp. 3434–3451, 2022. <https://doi.org/10.1109/TTE.2022.3221193>

- [23] H. Seo, J. Lim, G. H. Choe, J. Y. Choi, and J. H. Jeong, "Algorithm of linear induction motor control for low normal force of magnetic levitation train propulsion system," *IEEE Trans. Magn.*, vol. 54, no. 11, pp. 1–4, 2018. <https://doi.org/10.1109/TMAG.2018.2842222>
- [24] G. Lv, Z. Zhang, Y. Liu, and T. Zhou, "Analysis of forces in linear synchronous motor with propulsion, levitation and guidance for high-speed maglev," *IEEE J. Emerg. Sel. Top. Power Electron.*, vol. 10, no. 3, pp. 2903–2911, 2021. <https://doi.org/10.1109/JESTPE.2021.3065459>